CORA Cork Open Research Archive
Cartlann Taighde Oscailte Chorcaí

Title	Oxygen-vacancy induced ferroelectricity in nitrogen-doped nickel oxide
Authors	Dragoman, Mircea;Vulpe, Silviu;Aperathithis, Elias;Aivalioti, Chrysa;Romanitan, Cosmin;Dinescu, Adrian;Dragoman, Daniela;Aldrigo, Martino;Djourelov, Nikolay;Modreanu, Mircea;Moldovan, Antoniu
Publication date	2022-04-27
Original Citation	Dragoman, M., Vulpe, S., Aperathithis, E., Aivalioti, C., Romanitan, C., Dinescu, A., Dragoman, D., Aldrigo, M., Djourelov, N., Modreanu, M. and Moldovan, A. (2022) 'Oxygen-vacancy induced ferroelectricity in nitrogen-doped nickel oxide', Journal of Applied Physics, 131(16), 164304 (11pp). https://doi.org/10.1063/5.0075568
Type of publication	Article (peer-reviewed)
Link to publisher's version	10.1063/5.0075568
Rights	© 2022, the Authors. Published under an exclusive license by AIP Publishing. This article may be downloaded for personal use only. Any other use requires prior permission of the author and AIP Publishing. This article appeared as: Dragoman, M., Vulpe, S., Aperathithis, E., Aivalioti, C., Romanitan, C., Dinescu, A., Dragoman, D., Aldrigo, M., Djourelov, N., Modreanu, M. and Moldovan, A. (2022) 'Oxygen-vacancy induced ferroelectricity in nitrogen-doped nickel oxide', Journal of Applied Physics, 131(16), 164304 (11pp), doi: 10.1063/5.0075568 and may be found at https://doi.org/10.1063/5.0075568
Download date	2026-10-31 03:19:28
Item downloaded from	https://hdl.handle.net/10468/13136



University College Cork, Ireland
Coláiste na hOllscoile Corcaigh

Journal of Applied Physics

Oxygen-vacancy induced ferroelectricity in nitrogen-doped nickel oxide

Cite as: J. Appl. Phys. **131**, 164304 (2022); https://doi.org/10.1063/5.0075568
Submitted: 16 October 2021 • Accepted: 11 April 2022 • Published Online: 27 April 2022

Mircea Dragoman, Silviu Vulpe, Elias Aperathithis, et al.

COLLECTIONS

This paper was selected as Featured

View Online Export Citation CrossMark

ARTICLES YOU MAY BE INTERESTED IN

Acoustic phonons and elastic stiffnesses from Brillouin scattering of $CdPS_3$
Journal of Applied Physics **131**, 165109 (2022); https://doi.org/10.1063/5.0084258

Structure and relaxor ferroelectric behavior of the novel tungsten bronze type ceramic $Sr_5BiTi_3Nb_7O_{30}$
Journal of Applied Physics **131**, 164102 (2022); https://doi.org/10.1063/5.0084417

Observation of an anisotropic ultrafast spin relaxation process in large-area WTe_2 films
Journal of Applied Physics **131**, 163903 (2022); https://doi.org/10.1063/5.0090935

Lock-in Amplifiers up to 600 MHz
Zurich Instruments
Watch



© 2022 Author(s).

Journal of Applied Physics ARTICLE scitation.org/journal/jap

Oxygen-vacancy induced ferroelectricity in nitrogen-doped nickel oxide

Cite as: J. Appl. Phys. **131**, 164304 (2022); doi: 10.1063/5.0075568
Submitted: 16 October 2021 · Accepted: 11 April 2022 ·
Published Online: 27 April 2022

View Online Export Citation CrossMark

Mircea Dragoman,[1,a)] Silviu Vulpe,[1] Elias Aperathithis,[2] Chrysa Aivalioti,[2] Cosmin Romanitan,[1] Adrian Dinescu,[1] Daniela Dragoman,[3] Martino Aldrigo,[1] Nikolay Djourelov,[4] Mircea Modreanu,[5] and Antoniu Moldovan[6]

AFFILIATIONS

[1]National Institute for Research and Development in Microtechnologies (IMT Bucharest), Erou Iancu Nicolae Street 126A, 077190, Voluntari, Ilfov, Romania
[2]Microelectronics Research Group, Institute of Electronic Structure and Laser, Foundation for Research and Technology FORTH-Hellas, P.O. Box 1385, Heraklion 70013, Crete, Greece
[3]Physics Faculty, University of Bucharest, P.O. Box MG-11, 077125 Bucharest, Romania
[4]Extreme Light Infrastructure-Nuclear Physics (ELI-NP), "Horia Hulubei" National R&D Institute for Physics and Nuclear Engineering (IFIN-HH), 30 Reactorului Street, 077125 Magurele, Romania
[5]Tyndall National Institute-University College Cork, Lee Maltings, Dyke Parade, Cork T12 R5CP, Ireland
[6]National R&D Institute for Physics and Nuclear Engineering, 30 Reactorului Street, 077125 Magurele, Romania

[a)]**Author to whom correspondence should be addressed:** mircea.dragoman@imt.ro

ABSTRACT

This paper reports the onset of ferroelectricity in NiO by breaking the crystallographic symmetry with oxygen vacancies created by N doping. Nitrogen-doped NiO was grown at room temperature by RF sputtering of Ni target in $Ar–O_2–N_2$ plasma on silicon and fused silica substrates. The impact of the nitrogen doping of NiO on microstructural, optical, and electrical properties has been investigated. According to x-ray diffraction investigations, by increasing the N doping level in NiO, a transition from (002) to a (111) preferential orientation for the cubic NiO phase was observed, as well as a lattice strain relaxation, that is usually ascribed to structural defect formation in crystal. The x-ray diffraction pole figures the presence of a distorted cubic structure in NiO and supports the Rietveld refinement findings related to the strain, which pointed out that nitrogen doping fosters lattice imperfections formation. These findings were found to be in agreement with our far-infrared measurements that revealed that upon nitrogen doping a structural distortion of the NiO cubic phase appears. X-ray photoemission spectroscopy measurements reveal the presence of oxygen vacancies in the NiO film following nitrogen doping. Evidence of ferroelectricity in nitrogen-doped NiO thin films has been provided by using the well-established Sawyer–Tower method. The results reported here provide the first insights on oxygen-vacancy induced ferroelectricity in nitrogen-doped nickel oxide thin films.

Published under an exclusive license by AIP Publishing. https://doi.org/10.1063/5.0075568

I. INTRODUCTION

The search for new ferroelectric materials compatible with complementary metal–oxide–semiconductor (CMOS) technology is a hot topic of research since the integration of ferroelectrics in nanoelectronics circuits has many promising applications, such as low-power electronics, memories, neuromorphic computation, and energy harvesting.[1] Example in this respect are HfO_2-based ferroelectrics[2] obtained by doping with Zr, Y, Si, Ge, Al, and other dopants.[3] The memory applications of HfO_2-ferroelectrics are reviewed in Ref. 4, the applications of these materials for low-power electronics in the context of negative-capacitance transistors are reviewed in Refs. 5, 6, and 7, while HfO_2-ferroelectrics applications in microwaves, 2D materials ferroelectrics, 2D materials/HfO_2-ferroelectrics nanoelectronic devices, and energy harvesting are recently reviewed in Ref. 8. Besides, neuromorphic computations based on ferroelectric memristors are presented in Refs. 9 and 10. All these many applications of HfO_2-based ferroelectrics in

Published under an exclusive license by AIP Publishing

nanoelectronics are justifying the search for other CMOS-compatible ferroelectrics. Nickel oxide (NiO), which is a *p*-type semiconductor, is considered a suitable candidate for CMOS-compatible resistive switching memories (for a recent review, see Ref. 11) and memristors.[12] Besides these applications, NiO is also a ferromagnetic material and a transparent semiconductor, and Ni/NiO/Ni junctions are electromagnetic detectors, able to sense THz and infrared electromagnetic signals at room temperature.[13]

The fact that NiO doped with nitrogen (NiO:N) is a ferroelectric semiconductor as we report here has many implications. The advantages of a ferroelectric semiconductor are especially important since on a single chip we can combine various functions of semiconductors, such as amplification and digital processing, with those specific to ferroelectrics, such as memory. Therefore, on a single chip, it could be possible to assemble all electronic functions for in-memory computing, going thus beyond the von Neumann computing architecture used today, in which the memory and the digital processing unit (ALU) are separated, and the computer consumes the largest part of its electric power to transfer data between these two units.[14]

The discovery of 2D materials and their applications has renewed the interest in semiconductor ferroelectricity. An example in this sense is α-In_2Se_3, which is a semiconductor with mobility of 300–400 cm^2/Vs.[15] Other materials could also be of interest,[16] but their research is in infancy, i.e., ferroelectricity is proved using atomistic computations, and/or the experimental results are obtained from flakes. We have recently experimentally shown that semiconducting MoS_2 grown at the wafer-scale with a thickness of 4.5 nm has a ferroelectric phase induced by strain.[17]

In contrast, nitrogen-doped NiO reported here as a ferroelectrics semiconductor can be easily grown at the wafer-scale employing methods used by the microelectronics industry, for example, the Radio Frequency (RF) sputtering. We note that since the polarization is produced in the semiconductor there is a mobile charge that screens the depolarization, so any ferroelectric semiconductor has enhanced retention and endurance compared to insulator ferroelectrics such as HfO2-based ferroelectrics.[18]

In this paper, we report nitrogen-doped NiO films grown by RF Sputtering as a novel ferroelectric semiconductor material. A comprehensive approach involving complementary microstructural (x-ray diffraction and x-ray photoelectron spectroscopy), optical (UV–VIS–NIR spectrophotometry and Fourier transform infrared spectroscopy), and electrical characterization techniques (Sawyer–Tower method) were employed to obtain first insights on the ferroelectric mechanism phenomena in NiO:N thin films.

II. EXPERIMENTAL DETAILS

We have fabricated NiO:N films by RF sputtering of a 6-in. diameter Ni target in an Ar–O_2–N_2 plasma. All films were deposited at room temperature on both *p*-Si (100) *p*-type with the resistivity of 140 Ω cm and fused silica glass substrates. The glass substrates were cleaned in acetone and isopropanol, rinsed with de-ionized water, and dried in flowing nitrogen gas. The native oxide from the Si surface was removed by dipping them in a 10% HF solution for 30 s. Pre-cleaning of the target was performed for 15 min (Ar plasma, 5 mTorr, 300 W RF power). During deposition, the RF power was set at 300 W, the total pressure was kept at 5 mTorr, while the ratio of the flow rates of gases in plasma (non-reactive gas-Ar and reactive gases O_2 and N_2) were adjusted through a set of mass flow controllers (see experimental details in Table I, including the labeling of both nitrogen-doped and undoped samples). The NiO and NiO:N thin films thicknesses (see Table I) were measured by a Veeco Dektak 150 profilometer.

X-ray diffraction patterns were recorded using a 9 kW Rigaku SmartLab diffractometer in a medium-resolution mode. The applied voltage was 40 kV, while the current was 75 mA. To assess the effect of nitrogen doping level on the NiO microstructure, grazing incidence x-ray diffraction (GIXRD) was employed. To assure a good divergence of x rays, a PSA 0.5° soller slit was used at the detector. In this geometry, the incidence angle was kept at 0.5°, while the detector scanned from 10° to 90°. Figure 1 shows the GIXRD patterns (black points) for undoped and nitrogen-doped NiO thin films grown on both Si (100) (NN1, NN2, and NN6) and fused silica substrates (NN1*, NN2*, and NN6*).

Each x-ray diffraction pattern presents multiple diffraction peaks. These are found around 36.7, 42.4, 62.1, 74.4, and 77.1° and can be assigned unambiguously to (111), (002), (220), (311), and (222) NiO phases, according to the International Center for Diffraction Data (ICDD) database with card No. 001–1239 and cubic 225: Fm3m spatial group with $a = b = c = 0.42$ nm and $\alpha = \beta = \gamma = 90°$. Other diffraction peaks correspond to the substrate, namely, Si and fused silica. Also, x-ray diffraction data confirm the

TABLE I. Thickness and crystallite size as obtained from Scherrer's equation and Rietveld refinement, and the lattice strain for the investigated NiO:N samples were obtained at different ratios of gas flow.

Sample ID/sample type	Ratio of gas flow rates during RF growth	Substrate	Thickness (nm)	Crystallite size (nm)		Lattice strain (%)
				Scherrer	Rietveld	
NN1 (undoped NiO)	$\rho_{Ar}:\rho_{O2}:\rho_{N2} = 50:50:0$	Si	145 ± 5	5.24 ± 0.05	4.60	0.85
NN1* (undoped NiO)	$\rho_{Ar}:\rho_{O2}:\rho_{N2} = 50:50:0$	Fused silica	143 ± 5	5.07 ± 0.05	4.66	0.58
NN2 (NiO:N)	$\rho_{Ar}:\rho_{O2}:\rho_{N2} = 50:25:25$	Si	207 ± 5, 26 ± 2	9.14 ± 0.05	8.01	0.65
NN2* (NiO:N)	$\rho_{Ar}:\rho_{O2}:\rho_{N2} = 50:25:25$	Fused silica	196 ± 5	9.27 ± 0.05	7.22	0.56
NN6 (NiO:N)	$\rho_{Ar}:\rho_{O2}:\rho_{N2} = 25:25:50$	Si	258 ± 5	8.00 ± 0.05	6.62	0.53
NN6* (NiO:N)	$\rho_{Ar}:\rho_{O2}:\rho_{N2} = 25:25:50$	Fused silica	268 ± 5	8.68 ± 0.05	6.21	0.54

Published under an exclusive license by AIP Publishing

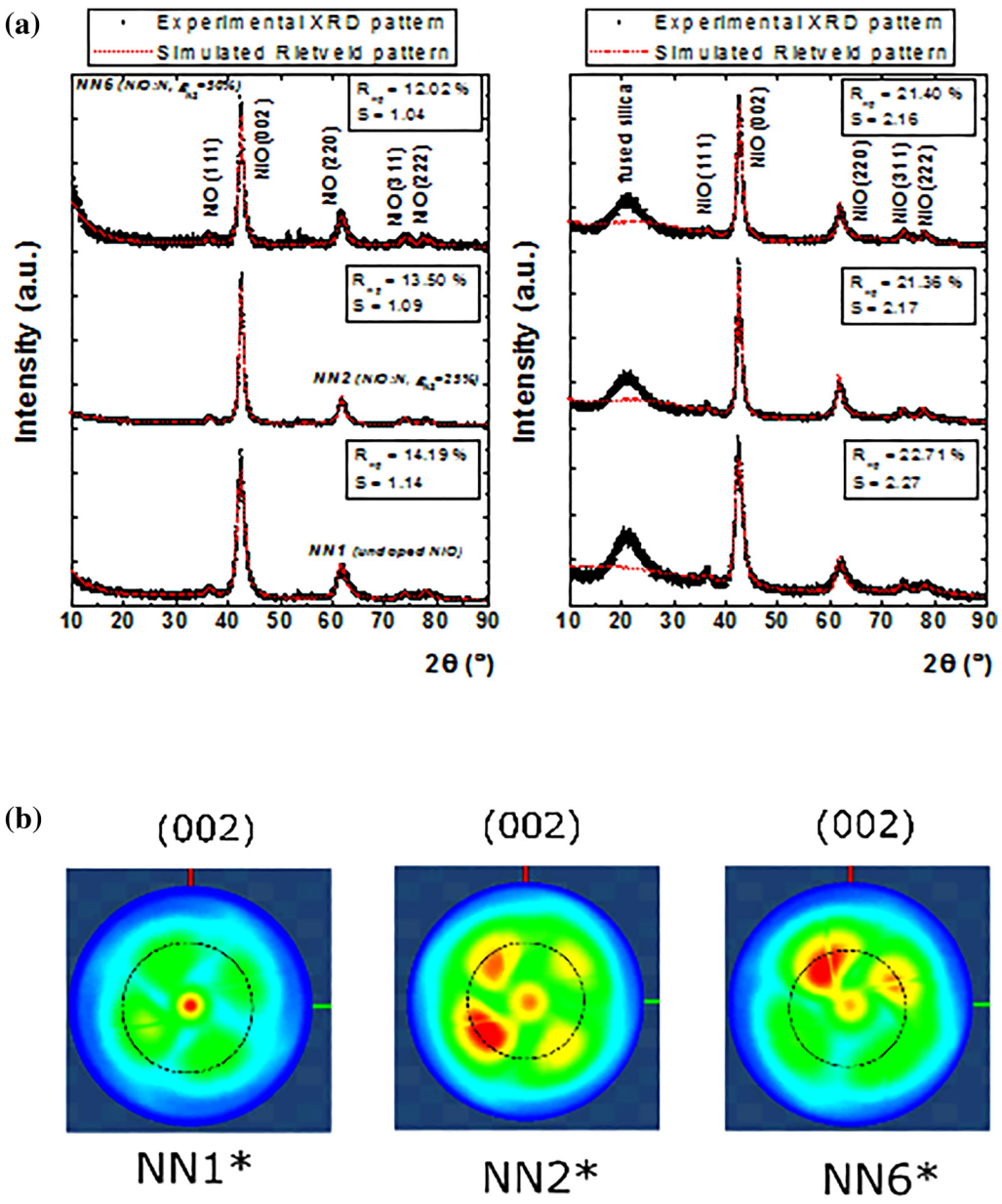


FIG. 1. (a) GIXRD patterns (black points) and the simulated profile (red line) in the framework of Rietveld refinement for undoped and nitrogen-doped NiO thin films grown by RF sputtering on Si (NN1, NN2, and NN6) and fused silica (NN1*, NN2*, and NN6*). The indexing of the diffraction peaks follows the ICDD database card ICDD No. 001–1239. (b) (002) pole figures on NiO thin films grown on fused silica (NN1*, NN2*, and NN6*). For the graphic representation was used 3D Explore software from Rigaku. The black dashed line stands to indicate the position of the pole figure spots.

purity of the samples, as no peak corresponding to secondary phases is present. Note that, usually, when a metal oxide is doped with N, a secondary phase like nickel nitride may occur.[19] The observed x-ray patterns reveal that pure and doped NiO show polycrystalline natures, the broadening of peaks revealing the formation of small crystalline domains.

To evaluate the size of the crystalline domains, the Scherrer formula was used. This gives the correlation between the peak

Published under an exclusive license by AIP Publishing

broadening and the mean crystallite size as[21] $\tau = k\lambda/\beta\cos(\theta)$, where k is the shape factor, usually taken as 0.9, $\lambda = 0.154$ nm is the wavelength of x rays, β is the full width at half maximum (FWHM) of the diffraction peak, and θ is the angular position of the diffraction peaks. According to the Scherrer formula, we found that the mean crystallite size increases on both substrates for N-doped samples (see Table I). For instance, in the case of the Si substrate, the mean crystallite size varies from 5.24 to 9.14 nm and 8.00 nm at higher N concentrations in the growth plasma while for the fused silica substrate, the corresponding mean crystallite sizes are 5.07, 9.27, and 8.68 nm. These results indicate an enhancement of crystallinity upon nitrogen doping, which is associated with a lower dislocation density, in agreement with an earlier report on the enhancement of crystallinity of NiOx films after N doping.[22] However, the Debye–Scherrer method considers only the effect of crystallite size on the diffraction peak broadening and does not bring information about the lattice strain.[23]

In this way, Rietveld full-profile refinement of the experimental x-ray diffraction pattern (red line) was performed to a quantitative description of the lattice distortion upon nitrogen doping. This method is based on the least squared fitting of a theoretical profile against the experimental one.[24] Briefly, the principle of the Rietveld Method lies in the minimization of a function M that accounts for the difference between a calculated profile y_i^{calc} and the observed data y_i^{obs}, with the following form:

$$M = \sum_i W_i \left\{ y_i^{obs} - \frac{1}{S} y_i^{calc} \right\}^2, \quad (1)$$

where W_i is the statistical weight and S is an overall scale factor such that $y_i^{calc} = S y_i^{obs}$. Here, S is the scale factor is a constant for a given phase and it is determined by the number, spatial distribution, and states of the scattering centers (atoms) in the unit cell.[25] More details regarding fitting parameters can be found in Ref. 26. In this model, each diffraction peak may be described by a symmetric, or nearly symmetric, pseudo-Voigt function, and the experimental line is fitted by a theoretical one. In particular, such kind of analysis is important taking into account that the size of the crystalline domains (called mean crystallite size) and the lattice strain govern the structural defects formation at the boundaries of the mosaic blocks. In Fig. 1(a), both the x-ray diffraction experimental profile (black curve) and fitted curve (red curve) are presented, with the corresponding fitting parameters determined using least squares fitting. In the case of the Si substrate, the S parameter, called the scale factor, is close to unity for each sample, while the weighted parameter (R_{wp}) varies from 12.02% to 14.19%. The relatively high R_{wp} value in our measurements is a result of quite a strong background noise. For the fused silica substrate, the parameters are higher, further indicating a worse fitting of the experimental data, mainly attributed to the fused silica substrate. The fitting parameters are listed in the inset of each figure.

After the simulation of the x-ray diffraction experimental pattern with the theoretical line, that encodes the crystal structure, it was obtained the crystallite size and lattice strain—Table I. The results derived from Rietveld refinement related to the mean crystallite size are strengthened by the Scherrer equation, both methods indicating the same trend of the mean crystallite size with the nitrogen doping. At the same time, each NiO lattice has a tensile strain, whose magnitude decreases as the nitrogen doping increases. For instance, the lattice strain decreases from 0.85% to 0.65%, reaching 0.53% on the Si substrate. At the same time, a decrease from 0.58% to 0.56%, reaching 0.54% in the case of the fused silica substrate, is suggested as a strain relaxation mechanism, driven by the doping in both cases. Usually, the strain relaxation processes are responsible for the structural defect formation in the crystal lattice.[27]

Additional insights about lattice symmetry and preferential orientation were gained using the pole figures recorded on (002) reflection. The pole figure was obtained by the inclination angle increment χ from 0° to 90° from the normal sample and for a full rotation of φ (0°–360°). In Fig. 1(b) are presented the pole figures on NiO thin films grown on fused silica (NN1*, NN2*, and NN6*). In the case of an undoped NiO sample, a central spot at $\chi = 0°$ and less intense four diffraction feature disposed on a circle (highlighted with a black dashed line) to a higher χ angle can be seen. Whereas the $\chi = 0°$ can be attributed to parallel atomic planes with the surface, namely, the [001] direction, the higher χ angle is rather attributed to an asymmetric atomic plane. Thus, a transition from (002) to (111) preferential orientation has taken place, contrary to Ref. 20, where a change from (111) to (002) directions was reported for doped NiO thin films. The high degree of disorder is shown by the broadening of the spots, and the different intensity of the spots is indicative that the cubic symmetry was altered.[28] In fact, pole figures support the Rietveld refinement findings related to the strain, where was pointed out that nitrogen doping fosters lattice imperfections formation.

Further, Fourier Transform Infrared (FTIR) measurements in the far-IR spectral range (50–600 cm^{-1}) have been performed in normal incidence for undoped and doped NiO samples deposited on Si using a Nicolet iS50 FTIR spectrometer equipped with a DLaTGS with polyethylene window detector and a Nicolet's solid beam splitter. The resolution was 4 cm^{-1} and 100 spectra have been co-added. The FTIR data have been analyzed and fitted with OMNIC software (Thermo Scientific). The far-IR spectra for the samples grown by RF sputtering on Si substrates are shown in Fig. 2. The main infrared phonon mode, centered on 400 cm^{-1}, was fitted with a Gaussian line shape and a representative fitted spectrum is illustrated with a dotted line in Fig. 2. A group analysis of the lattice modes of vibration at zero wavevector reveals two triply degenerate modes—three acoustic modes and three optical modes.[29] The optical modes are split into two degenerate transverse modes and one longitudinal mode. Because the rock salt structure has inversion symmetry, the optical modes have odd symmetry and thus can be seen in IR spectroscopy but not in Raman spectroscopy.

For the NiO's cubic rock salt structure, there is one IR active transverse optical (TO) phonon, ω_{TO}, due to Ni–O bond, which is reported in single-crystal NiO at $\omega_{TO} = 400 \pm 2$ cm^{-1}.[29] Here, we report the TO mode frequency for the polycrystalline undoped NiO (sample NN1) at 401 ± 0.5 cm^{-1}. The representative fitting spectra of the TO mode line shape for NN1 with a Gaussian are also shown. As follows from Fig. 2, after nitrogen doping of the NiO thin film, we see a systematic shift to lower infrared

Published under an exclusive license by AIP Publishing

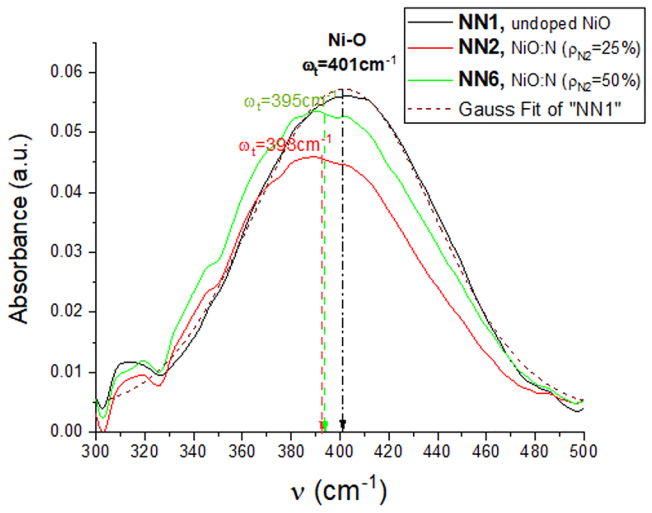


FIG. 2. FTIR spectra for IR active transverse optical (TO) phonon modes for undoped and nitrogen-doped NiO films.

frequencies for the TO mode: at $\omega_{TO} = 395 \pm 0.5\ cm^{-1}$ for the sample NN2 and at $\omega_{TO} = 393 \pm 0.5\ cm^{-1}$ for sample NN6. This shift is attributed here to atomic-scale distortions introduced by nitrogen doping that also lead to the formation of oxygen vacancies. Similar behavior was previously reported for other nitrogen-doped oxides such as ZnO. The vertical dotted lines show the TO phonon mode for NN1, NN2, and NN6 as obtained following the fitting procedure. These results concerning atomic-scale distortions

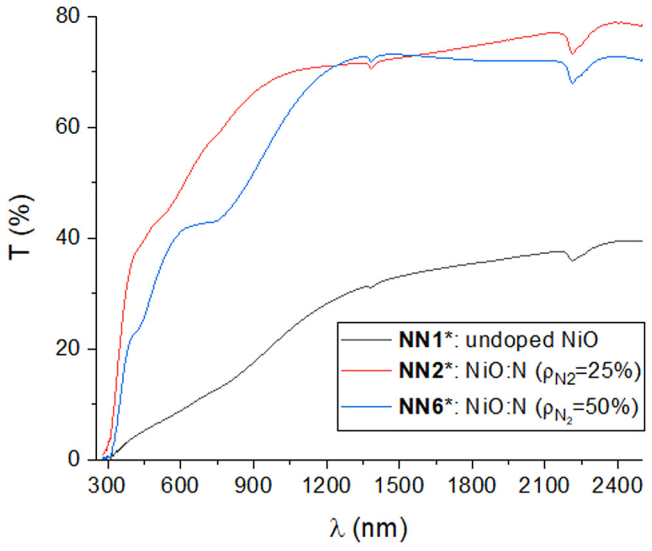


FIG. 3. UV–VIS–NIR optical transmittance spectra for the NiO:N samples NN1*, NN2*, and NN6* grown on fused silica substrates.

introduced by nitrogen doping are in good agreement with our XRD measurement and outline good IR spectroscopy capabilities in this respect that is rather unexploited.

UV–VIS–NIR optical transmission data have been acquired on NiO and NiO:N samples were grown by RF sputtering on the fused silica substrate (NN1*, NN2*, and NN6*) at normal incidence using an Agilent Carry 700 spectrometer and are shown in Fig. 3. Sample NN1* (undoped NiO) has the lowest optical transmission, while samples NN2* and NN6* show a significant enhancement of this parameter, which is associated with a better crystalline structure due to nitrogen doping; this result is in good agreement with the GIXRD results reported previously.

The absorption edges for NiO:N samples, NN2* and NN6*, extrapolated from the exponential decay of the optical transmission in the UV spectral range (for transmittance $\lesssim$15%) were found to be 3.67 ± 0.02 and, respectively, 3.42 ± 0.02 eV, both values being blue-shifted compared to the undoped NiO sample NN1*. This behavior could be possibly explained by the Burstein–Moss shift, which states that the apparent bandgap of a semiconductor increases, and the absorption edge is pushed to higher energies following the population/filling in of some states above the conduction band edge. In our case, the Burstein–Moss shift occurs due to nitrogen doping of NiO, in agreement with an earlier report[22] outlining that nitrogen doping improves the electrical conductivity of this material.

The GIXRD spectra from Fig. 1 show that the NiO:N microstructure is independent of the substrate used (Si or fused glass) for the same growth conditions (see Table I). As a consequence, the optical properties reported here for the samples grown on fused silica (NN1*, NN2*, and NN6*) are representative of the samples grown on the Si substrate (NN1, NN2, and NN6).

X-ray photoemission spectroscopy (XPS) spectra were recorded on a Sigma Surface Science photoelectron spectrometer equipped with a 160-mm hemispherical energy analyzer with a 1D detector (ASPECT) and using an Al K_α x-ray source at 13 kV at a power of 200 W. The analyzed area was $1.3 \times 1.3\ mm^2$, and the measurements have been performed on NiO and NiO:N thin films grown on Si. The pressure in the analysis chamber was kept below 1×10^{-9} mbar. Wide scan survey spectra were collected from −5 to 1200 eV (binding energy) with a constant pass energy of 160 eV. The high-resolution spectra of O 1s, Ni 2p3/2, and N 1s core levels were recorded using a pass energy of 50 eV. Since the N 1s signal was weak, the spectra were collected for ten-times longer acquisition time than the other high-resolution spectra. The sample normal coincided with the detection column axis. Under the same condition, the valence band was measured between 10 and −2 eV, and CasaXPS software was used for analysis. All spectra were calibrated such that the adventitious carbon C 1s main peak is at 284.8 eV. All spectra were fitted using a Shirley-type background and a Lorentzian asymmetric peak-shape [LA (1.53,243)]. Before the XPS measurements, the samples were infrared heated to ~100 °C for 5 min and etched for 2 min by 0.5 keV Ar+ with a current density of $\sim 5\ mA\ cm^{-2}$. The O 1s, Ni $2p_{3/2}$, and N1s XPS spectra for the samples NN1 and NN2 are shown in Fig. 4.

The O 1s core-level spectra can be decomposed into three components: (i) the first one at 529.4 ± 0.4 eV, attributed to oxygen atoms belonging to the Ni–O framework,[30] (ii) the second one at

Published under an exclusive license by AIP Publishing

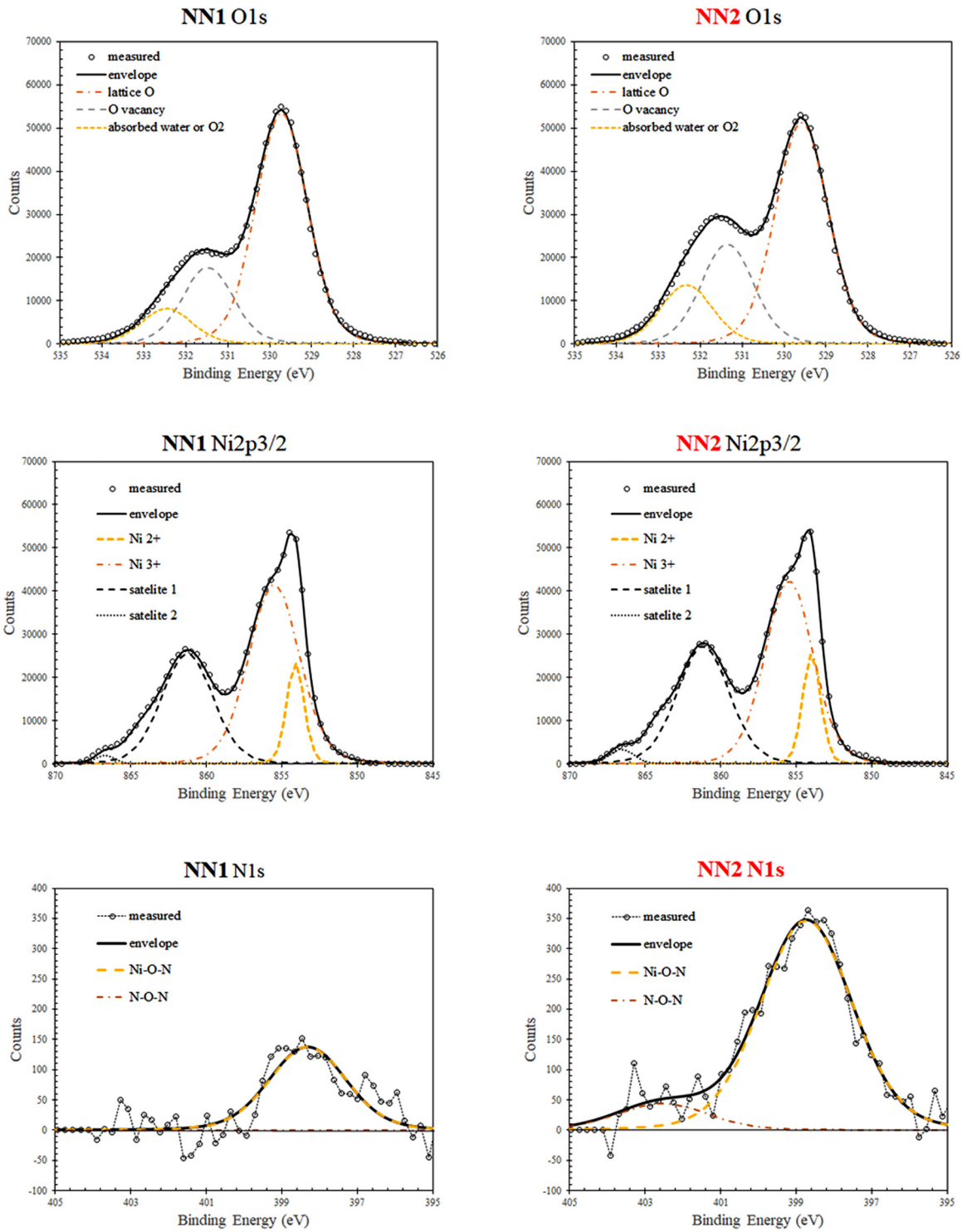


FIG. 4. XPS spectra for NiO:N samples: NN1 and NN2.

Published under an exclusive license by AIP Publishing

531.5 ± 0.4 eV, associated with oxygen vacancies in the Ni–O framework, and (iii) the third one at 532.8 ± 0.4 eV, attributed to oxygen from the OH group or water molecules.[31] It can be observed that for the sample NN2, the peak integral area of the second component of O 1s (attributed to oxygen vacancies in the Ni–O framework) increases as compared with that of the sample NN1 (undoped NiO). The increase of oxygen vacancies following doping is related to the incorporation of nitrogen in the Ni–O framework during the growth process.

Similarly, following the procedure reported previously in Ref. 32, the Ni $2p_{3/2}$ XPS spectra shown in Fig. 4 have four main components: (i) the first component at 853.9 ± 0.2 eV is attributed to Ni^{2+}; (ii) the second one at 855.5 ± 0.2 eV is conventionally assigned to the presence of Ni^{3+} species at the NiO surface since the intensity of this contribution was proven to show a dependence on the density of defects,[33] and (iii) two satellite peaks around 864 and 866 eV.[33] Our data suggest a 10% increase in the integral area ratio of $Ni^{3+}\backslash Ni^{2+}$ for the sample NN2 (NiO:N) with respect to the sample NN1, and this behavior is consistent with nitrogen incorporation in the Ni–O framework.

The N 1s spectra shown in Fig. 4 reveal that in the case of the sample NN2 (NiO:N) nitrogen was incorporated into the Ni–O framework mainly as Ni–O–N (assigned to the peak around 399 eV), but there is also evidence that a small amount of nitrogen is detected as N–O–N bound (associated to the peak found around 402.5 eV).[33] This fact also explains the increase of Ni^{3+} species, which is correlated to the creation of surface defects due to the formation of N–O–N bonds. It should be mentioned that there is nitrogen detected as Ni–O–N in the sample NN1 as well (a small amount, however, close to the XPS detection limit) due to the presence of residual nitrogen gas in the RF sputtering chamber. The presence of oxygen vacancy in NiO:N samples NN2 and NN6 is in agreement with FTIR results (the systematic shift to lower infrared frequencies for the TO mode due to oxygen vacancies and atomic-scale distortions introduced by nitrogen intercalation in the Ni–O matrix).

III. ELECTRICAL CHARACTERIZATION OF NIO:N SAMPLES

Electrical characterizations were carried out on tens of Cr/Au/NiO:N/doped Si structures. In detail for these electrical measurements, top metallic electrodes 5 nm-thick Cr/100 nm-thick Au with dimensions $150 \times 150\,\mu m^2$ have been deposited using a Temescal FC200 e-beam evaporation system (see Fig. 5).

The current–voltage dependence was measured using a Keithley SCS 4200 station, and the bottom electrode was assigned as a ground electrode. The electrical channels of the station are equipped with low-noise amplifiers connected to a probe station enclosed in a Faraday cage. All experiments were performed inside the probe station. No fitting algorithms were applied during or after measurements. The result, displayed in Fig. 6 for sample NN2 (comparable results were obtained for NN6 but not reported here), shows that we are dealing with a *p*-type semiconductor, as expected,[34] and several voltage sweeps used are confirming a clear and stable hysteresis.

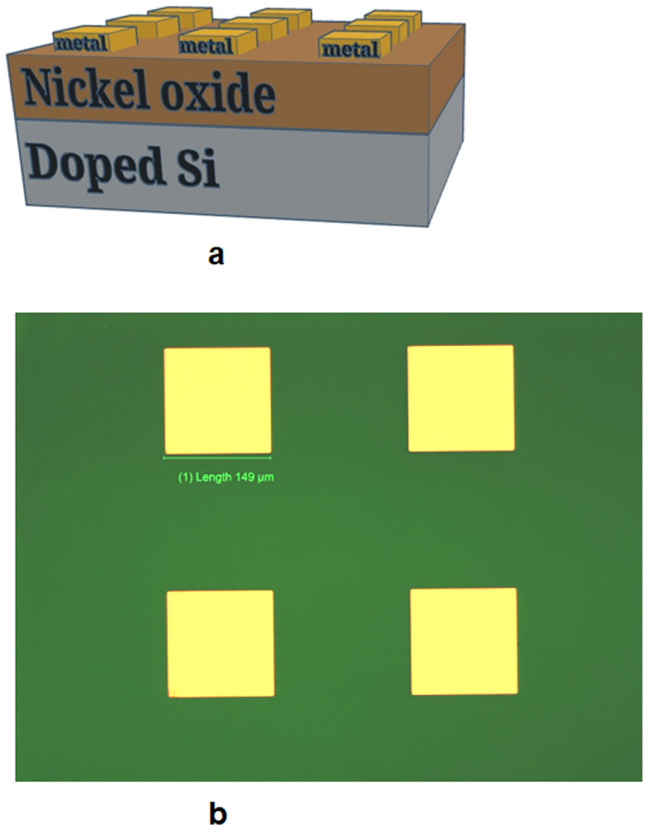


FIG. 5. (a) Schematic cross section of the NiO device and (b) optical image of the top electrodes.

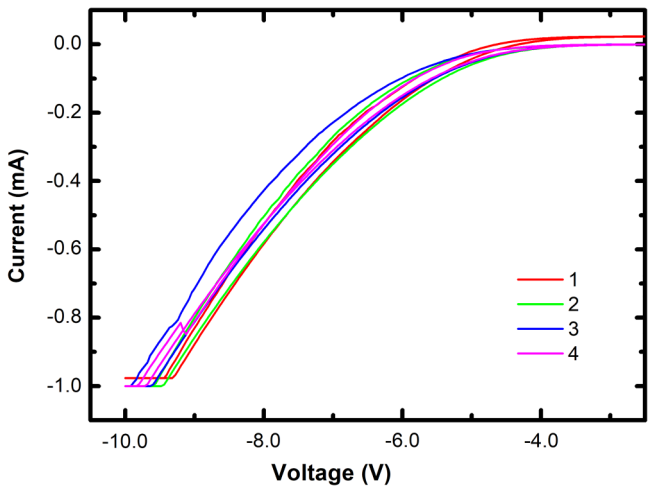


FIG. 6. Current–voltage dependence of the NN2 sample; the numbers in the inset represent the numbers of voltage sweeps.

Published under an exclusive license by AIP Publishing

The most straightforward proof of ferroelectricity is provided, however, by the $P(E)$ dependence, i.e., the dependence of the electrical polarization P on the applied DC field E. Generally, such measurements are performed for poled samples because, especially in polycrystalline materials, there is no net polarization in the absence of an applied electric field. However, when the top and bottom interfaces of an oxygen-deficient binary oxide thin film are different, as in our case (doped Si and metal), a built-in electric field could develop throughout the structure, which could generate a non-vanishing polarization even in the absence of an applied electric field. This is the reason we have investigated the $P(E)$ dependence of non-poled NiO:N samples. We have used the well-known Sawyer–Tower method for measuring $P(E)$ in different conditions.[35,36] The polarization–voltage (P–V) hysteresis loops were measured using a Sawyer–Tower circuit configuration consisting of a digital oscilloscope (Wavesurfer 3024—Teledyne LeCroy) and a pulse generator (NI PXIe-1078—National Instruments). To obtain (P–V) loops at different temperatures, a precision-controlled heating plate was used, which works up to 100 °C.

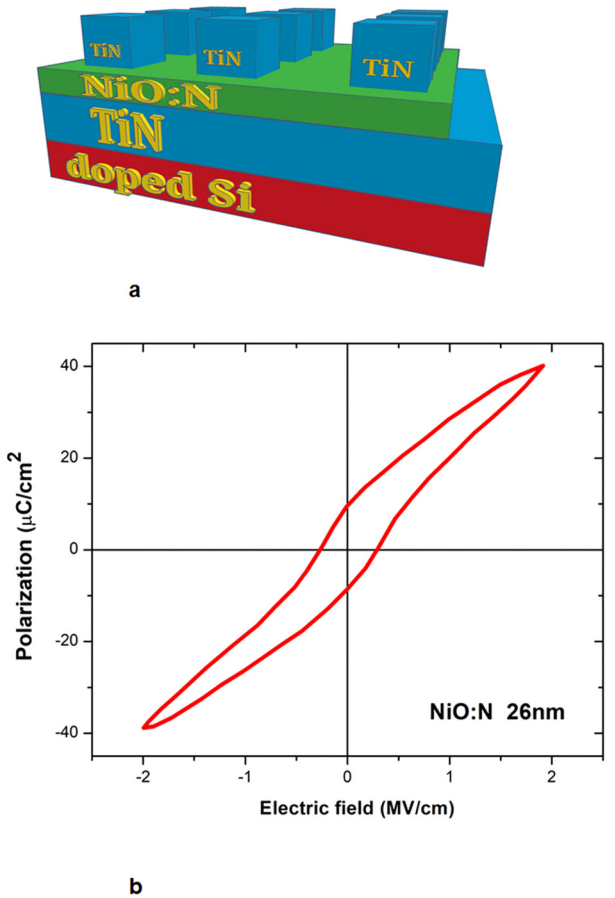


FIG. 7. (a) The TiN/NiO:N/TiN structure. (b) $P(E)$ for NN2 samples with the thickness of 26 nm at room temperature and 8 Hz.

However, $P(E)$ dependence does not show a typical ferroelectric electric polarization-field dependence at any studied temperature for all NiO:N samples although the prerequisites for ferroelectricity onset are established: a metastable distorted structure, a build-in field consistent with both different metallic electrodes,[37] and oxygen-vacancy induced dipole orientations.[38] The elliptic-like shapes of the $P(E)$ are specific for a leaky-capacitor because the conductivity of the NiO:N which is a semiconductor can diminish or even damage the ferroelectric features such as remanent polarization and/or saturation polarization.[39]

Therefore, we have grown in the same conditions as described above much thinner NN2 samples compared with the previous samples (NiO:N) on TiN which were previously deposited on doped Si and we have used as top electrodes also TiN. Thus, NiO:N samples are sandwiched between two TiN electrodes with a thickness of 50 nm and sheet resistance of 4 Ω/€ [see Fig. 7(a)]. The samples having a thickness of 45 nm did not show again a $P(E)$ shape that could be attributed to a ferroelectric. Thus, we have grown again NN2 samples with the thickness of 26 nm on doped Si to induce more strain in the structures able to deform much more the NiO:N atomic structure. The $P(E)$ dependence at room temperature is displayed in Fig. 7(b). The $P(E)$ curves are measured in the low current region up to −6 V, otherwise, the conductivity becomes too high and the significance of $P(E)$ is lost. We see that NiO:N is now ferroelectric showing a high coercive field of 1–2 MV/cm and a remanent polarization of 20 μC/cm^2 and a saturation polarization of 30 μC/cm^2 similar to HfO2-based ferroelectrics.[40] Thus, we have a semiconductor ferroelectric with ferroelectric parameters comparable to those of HfO_2-based ferroelectrics (insulators) or AlScN. Finally, we have grown in the same conditions NN2 samples with a thickness of 18 nm. The shape of the $P(E)$ dependence is preserved, but this time remanent polarization is smaller since the thickness is smaller (see Fig. 8). Thickness-induced ferroelectricity is a well-

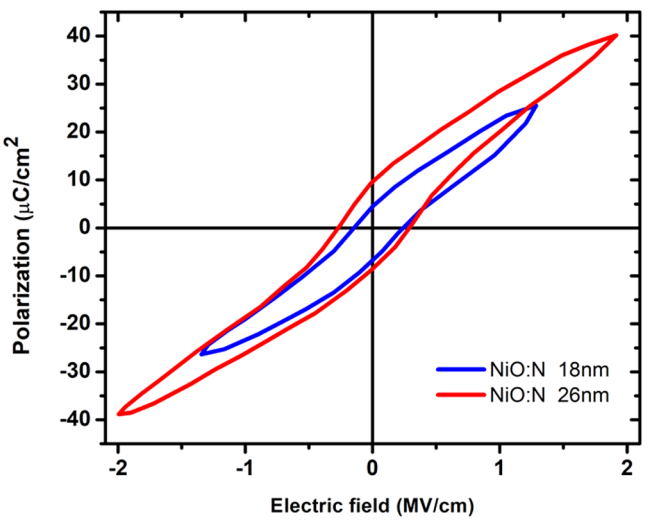


FIG. 8. $P(E)$ for NN2 samples with the thickness of 26 and 18 nm at room temperature and 8 Hz.

Published under an exclusive license by AIP Publishing

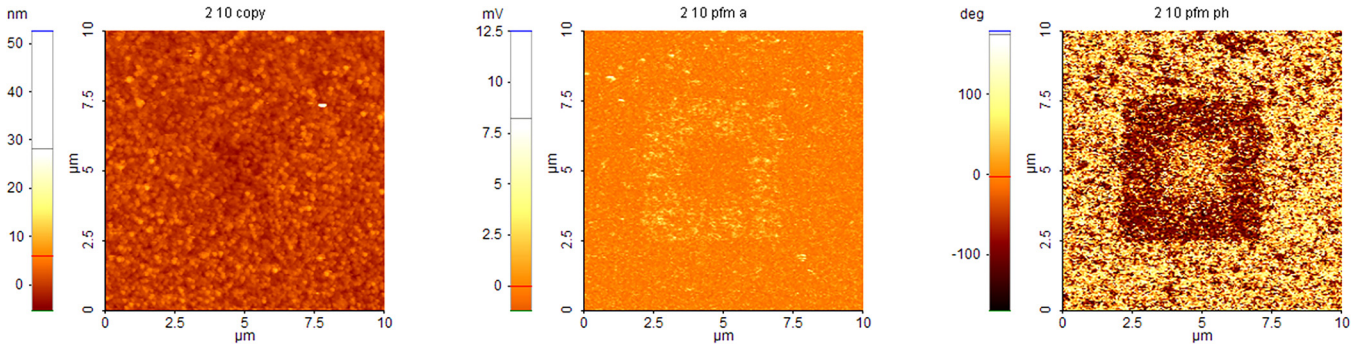


FIG. 9. AFM surface topography (left), PFM amplitude (center), and phase (right) response for the sample NN2.

known phenomenon studied intensively for many years in the area of ferroelectricity (see Ref. 41 and herein references) where in-plane strain stabilizes the out-of-plane ferroelectricity. The same mechanism is responsible for the occurrence and stabilization of ferroelectricity in HfO_2-ferroelectrics.[42] TiN electrodes play the same role as in the case HfO_2-based oxides, i.e., the stabilization of the ferroelectricity in the structure. We have progressively increased the temperature of the sample and we have observed the $P(E)$ curve behavior at 90 °C the $P(E)$ is vanishing.

The piezoresponse force microscopy (PFM) was also used for the investigation of ferroelectricity in NiO:N (samples NN2 and NN6) and NiO films (sample NN1). To evidence the ferroelectric behavior of the samples by PFM measurements, an area of $5 \times 5\,\mu m^2$ was scanned with +5 V bias applied to the substrate, while for the small square ($2 \times 2\,\mu m^2$), −5 V bias was applied to the substrate; the tip was held at ground potential. While all other samples have no characteristic ferroelectric response in PFM, NN2 samples show a ferroelectric response in PFM as shown in Fig. 9. The phase images (Fig. 9, right) show a reversal of the local polarization of the material for areas where the applied electric field had opposite directions.

The fact that we have seen ferroelectricity only in the oxygen-deficient N-doped samples (as was shown by XPS measurements) comes as no surprise. Indeed, numerical calculations have shown that ferroelectricity in binary oxide thin films, and generally multiferroicity is related to oxygen vacancies.[43] In this case, oxygen vacancies, as elastic dipoles, can be partially transformed into electric dipoles due to symmetry-breaking interfaces and defects (including grain boundaries in the case of polycrystalline samples), around which vacancies tend to accumulate by diffusing through the sample. NiO ionized oxygen vacancies are highly susceptible to form clusters.[34] Besides, N impurities could promote the generation of oxygen vacancies and combine with them to enhance ferroelectricity. First-principle calculations have confirmed this behavior in HfO_2-based ferroelectrics.[44] Summarizing, local electric fields are generated around the symmetry-breaking surface or point defects, extending on distances of up to micrometers,[45] carefully designed heterointerfaces supplying a method to generate ferroelectricity in otherwise non-ferroelectric oxides.[46] The electrical measurements reported in the following strengthen the conclusion that oxygen-deficient NiO:N is ferroelectric.

IV. CONCLUSIONS

The results reported here provide the first insights on oxygen-vacancy induced ferroelectricity in nitrogen-doped nickel oxide thin films grown RF sputtering at room temperature.

Our results indicate that the nitrogen doping of NiO introduces not only atomic-scale distortion (as revealed by the Rietveld refinement and XRD pole figures and by the systematic shift to lower infrared frequencies for the Ni–O TO mode) but also favors the appearance of oxygen vacancies in NiO films (as demonstrated by XPS measurements).

The results presented here provide a strong indication that the onset of ferroelectricity in NiO is due to the breaking of its centrosymmetry by oxygen vacancies created by N doping. Our findings represent an important example of the symmetry breaking of materials to create new functionalities of the same materials unknown before. Very recently, giant piezoelectricity was reported in Gd doped CeO_2 films by controlled oxygen vacancies generation.[47] We mention also the symmetry breaking of centrosymmetric semiconductors and the occurrence of piezoelectricity and pyroelectricity by built-in electric fields created by Schottky contacts.[48] So, this is an important route to create new piezoelectric and ferroelectric materials to be compatible with CMOS technology since the most known materials having such physical properties are either not compatible with CMOS technology or have serious reliability problems like HfO_2-based ferroelectrics.

ACKNOWLEDGMENTS

This work was supported by European Union's Horizon 2020 FETPROACT Grant Agreement No. 951761, "Nanomaterials enabling smart energy harvesting for next-generation Internet-of-Things" (NANO-EH). It was also partly supported by the Extreme Light Infrastructure Nuclear Physics (ELI-NP) Phase II, a project co-financed by the Romanian Government and the European Union through the European Regional Development Fund and the Competitiveness Operational Program (1/07.07.2016, ID 1334) and "Materials and Processes for Energy and Environment Applications-AENAO" (MIS 5002556) and "NANOTANDEM" (MIS 5029191) co-financed by Greece and EU (European Regional Development Fund).

Published under an exclusive license by AIP Publishing

AUTHOR DECLARATIONS

Conflict of Interest

The authors have no conflicts to disclose.

DATA AVAILABILITY

The data that support the findings of this study are available from the corresponding author upon reasonable request.

REFERENCES

[1]H. Ryu, K. Xu, D. Li, X. Hong, and W. Zhu, "Empowering 2D nanoelectronics via ferroelectricity," Appl. Phys. Lett. **117**, 080503 (2020).
[2]J. Müller, T. S. Böscke, U. Schröder, S. Mueller, D. Braühaus, U. Böttger, L. Frey, and T. Mikolajick, "Ferroelectricity in simple binary ZrO_2 and HfO_2," Nano Lett. **12**, 4318–4323 (2012).
[3]M. H. Park, Y. H. Lee, H. J. Kim, Y. J. Kim, T. Moon, K. D. Kim, J. Muller, A. Kersch, U. Schroeder, T. Mikolajick, and C. S. Hwang, "Ferroelectricity and antiferro-electricity of doped thin HfO_2-based films," Adv. Mater. **27**, 1811 (2015).
[4]M. H. Park, Y. H. Lee, T. Mikolajick, U. Schroeder, and C. S. Hwang, "Review and perspective on ferroelectric HfO_2-based thin films for memory applications," MRS Commun. **8**, 795 (2018).
[5]M. A. Alam, M. Si, and P. D. Ye, "A critical review of recent progress on negative capacitance field-effect transistors," Appl. Phys. Lett. **114**, 090401 (2019).
[6]M. Hoffmann, S. Slesazeck, U. Schroeder, and T. Mikolajick, "What's next for negative capacitance electronics?," Nat. Electron. **3**, 504 (2020).
[7]J. C. Wong and S. Salahuddin, "Negative capacitance transistors," Proc. IEEE **107**, 49 (2019).
[8]M. Dragoman, M. Aldrigo, D. Dragoman, S. Iordanescu, A. Dinescu, and M. Modreanu, "HfO_2-based ferroelectrics applications in nanoelectronics," Phys. Status Solidi RRL **15**, 2000521 (2021).
[9]S. Oh, H. Hwang, and I. K. Yoo, "Ferroelectric materials for neuromorphic computing," APL Mater. **7**, 091109 (2019).
[10]M. Dragoman and D. Dragoman, *Atomic-scale Electronics Beyond CMOS* (Springer, Cham, 2021), Chap. 5.
[11]E. Carlos, R. Branquinho, R. Martins, A. Kiazadeh, and E. Fortunato, "Recent progress in solution-based metal oxide resistive switching devices," Adv. Mater. **32**, 2004328 (2020).
[12]Y. Li, Z. Wang, R. Midya, Q. Xia, and J. J. Yang, "Review of memristor devices in neuromorphic computing: Materials sciences and device challenges," J. Phys. D: Appl. Phys. **51**, 503002 (2018).
[13]P. C. D. Hobbs, R. B. Laibowitz, and F. R. Libsch, "Ni–NiO–Ni tunnel junctions for terahertz and infrared detection," Appl. Opt. **44**, 6813–6822 (2005).
[14]E. T. Breyer, H. Mulaosmanovic, T. Mikolajick, and S. Slesazeck, "Perspective on ferroelectric, hafnium oxide based transistors for digital beyond von-Neumann computing," Appl. Phys. Lett. **118**, 050501 (2021).
[15]M. Si, A. K. Saha, S. Gao, G. Qiu, J. Qin, Y. Duan, J. Jian, C. Niu, H. Wang, W. Wu, S. K. Gupta, and P. D. Ye, "A ferroelectric semiconductor field-effect transistor," Nat. Electron. **2**, 580–586 (2019).
[16]Z. Guan, H. Hu, X. Shen, P. Xiang, N. Zhong, J. Chu, and C. Duan, "Recent progress in two-dimensional ferroelectric materials," Adv. Electron. Mater. **6**, 1900818 (2020).
[17]M. Dragoman, M. Aldrigo, D. Dragoman, I. M. Povey, S. Iordanescu, A. Dinescu, A. Di Donato, and M. Modreanu, "Multifunctionalities of 2D MoS_2 self-switching diode as memristor and photodetector," Physica E **126**, 114451 (2021).
[18]J. Y. Kim, M. J. Choi, and H. W. Jang, "Ferroelctric field transistors: Progress and perspectives," APL Mater. **9**, 021102 (2021).
[19]F. Gillot, J. Oró-Solé, and M. R. Palacín, "Nickel nitride as negative electrode material for lithium ion batteries," J. Mater. Chem. **21**, 9997–10002 (2011).
[20]S. Sriram, A. Thayumanavan, and K. Ravichandran, "Influence of nitrogen doping on properties of NiO films," Surf. Eng. **32**, 207–211 (2016).
[21]A. L. Patterson, "The Scherrer formula for x-ray particle size determination," Phys. Rev. **56**, 978–982 (1939).
[22]P. Zhou, B. Li, Z. Fang, W. Zhou, M. Zhang, W. Hu, T. Chen, Z. Xiao, and S. Yang, "Nitrogen-doped nickel oxide as hole transport layer for high-efficiency inverted planar perovskite solar cells," Solar RRL **3**, 1900164 (2019).
[23]D. Nath, F. Singh, and R. Das, "X-ray diffraction analysis by Williamson-Hall, Halder-Wagner and size-strain plot methods of CdSe nanoparticles—A comparative study," Mater. Chem. Phys. **239**, 122021 (2020).
[24]H. M. Rietveld, "A profile refinement method for nuclear and magnetic structures," J. Appl. Crystallogr. **2**, 65–71 (1969).
[25]L. Lutterotti, "Total pattern fitting for the combined size-strain-stress-texture determination in thin film diffraction," Nucl. Instrum. Methods Phys. Res. B **268**, 334–340 (2010).
[26]V. K. Pecharsky and P. Y. Zavalij, *Fundamentals of Powder Diffraction and Structural Characterization of Materials*, 2nd ed. (Springer, New York, 2009).
[27]C. Romanitan, I. V. Tudose, K. Mouratis, M. C. Popescu, C. Pachiu, S. Couris, E. Koudoumas, and M. Suchea, "Structural investigations in electrochromic vanadium pentoxide thin films," Phys. Status Solidi A 2100431 (Published online 2022).
[28]K. Bowen and B. Tanner, *High Resolution X-Ray Diffractometer and Topography* (Taylor & Francis, London, 1998).
[29]D. J. Lockwood, G. Yu, and N. L. Rowell, "Oblique incidence infrared reflectance spectroscopy of phonons in cubic MgO, MnO, and NiO," Infrared Phys. Technol. **109**, 103405 (2020).
[30]M. C. Biesinger, B. P. Payne, L. W. M. Lau, A. Gerson, and R. St. C. Smart, "X-ray photoelectron spectroscopic chemical state quantification of mixed nickel metal, oxide and hydroxide systems," Surf. Interface Anal. **41**, 324–332 (2009).
[31]Y. Gao, Y. Masuda, and K. Koumoto, "Light-excited superhydrophilicity of amorphous TiO_2 thin films deposited in an aqueous peroxotitanate solution," Langmuir **20**, 3188–3194 (2004).
[32]J. Keraudy, A. Ferrec, M. Richard-Plouet, J. Hamon, A. Goullet, and P.-Y. Jouan, "Nitrogen doping on NiO by reactive magnetron sputtering: A new pathway to dynamically tune the optical and electrical properties," Appl. Surf. Sci. **409**, 77–84 (2017).
[33]St. Uhlenbrock, C. Scharfschwerdt, M. Neumann, G. Illing, and H.-J. Freund, "The influence of defects on the Ni 2p and O 1s XPS of NiO," J. Phys. Condens. Matter **4**, 7973 (1992).
[34]S. Park, H.-S. Ahn, C.-K. Lee, H. Kim, H. Jin, H.-S. Lee, S. Seo, J. Yu, and S. Han, "Interaction and ordering of vacancy defects in NiO," Phys. Rev. B **77**, 134103 (2008).
[35]C. B. Sawyer and C. H. Tower, "Rochelle salt as dielectric," Phys. Rev. **35**, 269–273 (1930).
[36]X. Qiu, L. Holländer, W. Wirges, R. Gerhard, and H. C. Basso, "Direct hysteresis measurements on ferroelectric films by means of a modified Sawyer–Tower circuit," J. Appl. Phys. **113**, 224106 (2013).
[37]J. J. Lee and S. B. Desu, "The shifting of P-E hysteresis loop by the asymmetric contacts on ferroelectric PZT thin films," Ferroelectr. Lett. Sect. **20**, 27–34 (1995).
[38]E. Sapper, R. Dittmer, D. Damjanovic, E. Erdem, D. J. Keeble, W. Jo, T. Granzow, and J. Rödel, "Aging in the relaxor and ferroelectric state of Fe-doped (1-x)$(Bi_{1/2}Na_{1/2})TiO_3$-x$BaTiO_3$ piezoelectric ceramics," J. Appl. Phys. **116**, 104102 (2014).
[39]L. Jin, F. Li, and S. Zhang, "Decoding the fingerprint of ferroelectric loops: Comprehension of the material properties and structures," J. Am. Ceram. Soc. **97**(1), 1–27 (2014).
[40]T. Shimizu, T. Yokouchi, T. Oikawa, T. Shiraishi, T. Kiguchi, A. Akama, T. J. Konno, A. Gruverman, and H. Funakubo, "Contribution of oxygen vacancies to the ferroelectric behavior of $Hf_{0.5}Zr_{0.5}O_2$ thin films," Appl. Phys. Lett. **106**, 112904 (2015).
[41]L. J. Sinnamon, R. M. Bowman, and J. M. Gregg, "Thickness-induced stabilization of ferroelectricity in $SrRuO_3$/$Ba_{0.5}Sr_{0.5}Ti_{O3}$/Au thin film capacitors," Appl. Phys. Lett. **81**, 889 (2002).

Published under an exclusive license by AIP Publishing

[42]T. Shimizu, "Ferroelectricity in HfO_2 and related ferroelectrics," J. Ceram. Soc. Jpn. **126**, 667 (2018).
[43]M. D. Glinchuk, A. N. Morozovska, and L. P. Yurchenko, "Origin of ferroelectricity and multiferroicity in binary oxide thin films," IEEE Trans. Ultrason. Ferroelect. Freq. Control **68**, 273–278 (2021).
[44]Y. Zhou, Y. K. Zhang, Q. Yang, J. Jiang, P. fan, M. Liao, and Y. C. Zhou, "The effects of oxygen vacancies on ferroelectric phase transition of HfO_2-based thin film from first-principle," Comput. Mater. Sci. **167**, 143–150 (2019).
[45]J. Zhu, J.-W. Lee, H. Lee, L. Xie, X. Pan, R. A. De Souza, C.-B. Eom, and S. S. Nonnenmann, "Probing vacancy behavior across complex oxide heterointerfaces," Sci. Adv. **5**, 8467 (2019).
[46]R. He, J. L. Lin, Q. Liu, Z. Liao, L. Shui, Z. J. Wang, Z. Zhong, and R.-W. Li, "Emergent ferroelectricity in otherwise nonferroelectric oxides by oxygen vacancy design at heterointerfaces," ACS Appl. Mater. Interfaces **12**, 45602–45610 (2020).
[47]D. S. Park1, M. Hadad, L. M. Riemer, R. Ignatans, D. Spirito, V. Esposito, V. Tileli, N. Gauquelin, D. Chezganov, D. Jannis, J. Verbeeck, S. Gorfman, N. Pryds, P. Muralt, and D. Damjanovic, "Induced giant piezoelectricity in centrosymmetric oxides," Science **375**, 653–657 (2022).
[48]M.-M. Yang, Z.-D. Luo, Z. Mi, J. Zhao, S. Pei E, and M. Alexe, "Piezoelectric and pyroelectric effects induced by interface polar symmetry," Nature **584**, 377 (2020).

Published under an exclusive license by AIP Publishing